Operating Point Optimization of Auxiliary Power Unit Based on Dynamic Combined Cost Map and Particle Swarm Optimization

Yaonan Wang, Yongpeng Shen, Xiaofang Yuan, and Yimin Yang

***Abstract*—Series hybrid electric vehicles improvements in fuel consumption and emissions directly depend on the operating point of the auxiliary power unit (APU). A new APU operating point optimization approach based on dynamic combined cost map (DCM) and particle swarm optimization (PSO) is presented in this paper. The influence of coolant temperature, catalyst temperature, and air/fuel (A/F) ratio on fuel consumption characteristics and HC, CO, NOx emission characteristics are quantitatively analyzed first. Then, the DCM is derived by combining the individual cost maps with predefined weighting factors, so as to balance the potentially conflicting goals of fuel consumption and emissions reduction in the choice of operating point. The PSO is utilized to search the optimum APU operating point in the DCM. Finally, bench experiments under three typical driving cycles show that, compared with the results of the traditional static steady-state fuel consumption map-based APU operating point optimization approach, the proposed DCM and PSO-based approach shows significant improvements in emission performance, at the expense of a slight drop in fuel efficiency.**

***Index Terms*—Auxiliary power unit (APU), emissions, fuel consumption, particle swarm optimization (PSO), series hybrid electric vehicles (SHEVs).**

I. INTRODUCTION

AIR POLLUTION, global warming, and petroleum resource depletion issues associated with the development of modern transportation are now problems of paramount concern. Progressively, more rigorous emissions and fuel efficiency standards are stimulating the aggressive development of safer, cleaner, and more efficient vehicles [1]. Hybrid electric vehicles (HEVs) have attracted much attention in the last few years due to their inherent advantages of improved fuel efficiency and reduced hazardous emissions. Among three basic kinds of HEVs (series, parallel and series–parallel), the series hybrid electric vehicle (SHEV) is a promising solution for next-generation ground vehicle due to its outstanding transient performance and simple architecture [2].

Improvements in fuel economy and emissions of SHEVs strongly depend on the supervisory control strategies [3]. On one hand, the supervisory control strategy determines the power distribution between auxiliary power unit (APU) and power battery, so that the power requirement of the driver is satisfied and the state of charge (SOC) of the battery is maintained in a preset window. On the other hand, the supervisory control strategy is responsible for operating the APU with optimum fuel efficiency and emissions. To improve the fuel efficiency and emissions of the SHEVs, several approaches have been proposed.

Barsali *et al.* [4] proposed a novel approach to minimize the fuel consumption of the SHEVs. Through optimizing the ON/OFF strategy and instantaneous output power of the generator, this approach shows fuel efficiency improvements between 1.6% and 1.5% compared with the thermostat control strategy. Furthermore, in order to maximize the vehicle efficiency, Barsali *et al.* also proposed a load forecast algorithm to forecast the future load of the vehicle in [5]. Gokasan *et al.* [6] proposed a novel approach in the optimization of APU fuel efficiency. Two chattering-free sliding-mode controllers (SMCs) were developed to keep the engine operating in the optimal efficiency region, whenever the engine operation is required due to a drop in the SOC level. One of the SMCs adjusts the engine throttle to maintain the engine speed at a certain level, while the other performs engine/generator torque control via the power converter, so that the engine works in the optimal efficiency region, despite load variations. Similar approaches include [7]–[10]. Nino-Baron *et al.* [11] proposed a methodology of calculating the optimal torque and speed commands for the APU of an SHEV based on maximal principle, which maximizes the total system efficiency while producing the requested target energy in a requested time interval. The APU operation during the transient, the system mechanical dynamics, and the torque limitations of the engine and generator were considered in this paper. For more details about different approaches in improving fuel efficiency and emissions of SHEVs, see [12]–[15].

One of the general characteristics of the aforementioned approaches is that they attempt to improve the fuel efficiency and emissions simultaneously just based on the steady-state fuel efficiency map (SFM) of the engine. However, on the speed–torque map of an ICE, the locus of maximum fuel efficiency does not necessarily correspond to the loci of optimum emissions. In some cases, they are even two sections in the map of optimum performance [16]. In other words, the operating point with

Manuscript received September 10, 2014; revised November 10, 2014; accepted December 5, 2014. Date of publication December 18, 2014; date of current version August 21, 2015. This work was supported by the National High Technology Research and Development Program of China (863 Program) (No. 2012AA111004) and National Natural Science Foundation of China (No. 61104088). Recommended for publication by Associate Editor S. Williamson.

Y. Wang, Y. Shen, and X. Yuan are with the Department of Electric and Information Engineering, Hunan University, Changsha 410082, China (e-mail: yaonan@hnu.edu.cn; shenyongpeng@hnu.edu.cn; yuanxiaofang@hnu.edu.cn).

Y. Yang is with the College of Electric Engineering, Guangxi University, Nanning 530004, China, and also with the Department of Electrical and Computer Engineering, University of Windsor, Windsor, ON N9B 3P4, Canada (e-mail: eyyang@uwindsor.ca).

Color versions of one or more of the figures in this paper are available online at http://ieeexplore.ieee.org.

Digital Object Identifier 10.1109/TPEL.2014.2383443

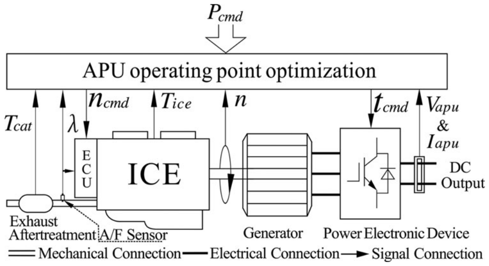

Fig. 1. Schematic of the APU.

minimum fuel consumption (FC) does not necessarily result in the minimum emissions. In addition, the transient FC and emissions not only depend on the steady-state fuel efficiency and emission characteristics, but also depend on the engine coolant temperature correction factors and three-way catalyst converter (TWC) removal efficiency (varying with catalyst temperature and air/fuel (A/F) ratio) [17]. The challenge for the control strategy is how to balance the goals of higher fuel efficiency and lower emissions simultaneously, and meanwhile, take into account the influence of the engine coolant temperature, TWC temperature, and A/F ratio on the characteristics of fuel efficiency and emissions.

Unlike the aforementioned control strategies that employ the isolated steady-state speed–torque (power)-SFM and show little sensitivity to subtle emissions tradeoffs, as one of the main contributions of this paper, the dynamic combined cost map is derived by combining the individual cost maps of FC, HC (Hydrocarbons), CO (Carbon Monoxide), NOx (Nitrous Oxides), and PM (Particulate Matter) with predefined weighting factors. At the same time, the influence of coolant temperature, TWC temperature, and A/F ratio on FC and emissions are all considered in the proposed approach.

As another contribution, the particle swarm optimization (PSO) is introduced for searching the optimum APU operating point under three kinds of constraints: 1) searching the optimum operating point in the whole DCM; 2) searching the optimum operating point in a specific power interval; and 3) searching the optimum operating point of a specific power.

This paper is organized as follows. In Section II, the APU operating point optimization problem is described in detail. In Section III, the influence of temperature and A/F ratio on FC, emissions, and catalysts behavior is analyzed. The normalization and weighting operation of the dynamic combined cost map are also discussed in this section. Section IV describes the principle and implementation steps of the PSO. Three kinds of constraints are also discussed in this section. In Section V, bench experiments are carried out over three typical driving cycles, and comparisons are made between the results of the proposed approach and that of the baseline SFM-based approach. Finally, the conclusion is stated in Section VI.

II. PROBLEM STATEMENT

The structure of the APU investigated in this paper is shown in Fig. 1. It consist of an ICE, an exhaust after-treatment device (TWC), a generator (permanent magnet synchronous machine (PMSM) or induction machine), and a power electric device (acts as motor controller and rectifier).

A common shaft connects the ICE and generator directly. In the start-up phase, the generator acts as a starting motor, while in the other working phase, it acts as a battery charger. The APU operating point optimization program is embedded in the APU controller; it determines the operating point of the APU $(n_{\mathrm{cmd}}, t_{\mathrm{cmd}})$ according to the power demands instruction P_{cmd} from high-level supervisory control strategies. At the same time, the real-time APU working information, such as catalyst temperature T_{cat}, normalized A/F ratio λ ($\lambda = \frac{\mathrm{A/F}}{14.67}$, where 14.67 is the ideal stoichiometric value of A/F ratio), coolant temperature T_{ice}, APU rotate speed n, dc output voltage V_{apu}, and current I_{apu} are input parameters of the APU operating point optimization approach. In this paper, the catalyst temperature T_{cat} and coolant temperature T_{ice} are sensed by two temperature sensors; the A/F ratio λ is sensed by a universal exhaust gas oxygen sensor. These signals are processed by an AutoBox, which acts as an APU controller and implements the APU operating point optimization approach in the experiment.

The fuel efficiency and emissions of the APU are strongly dependent on the operating point of the APU, regardless of which kind of high-level supervisory control strategy is utilized. However, the speed–torque/power–fuel efficiency characteristics and speed–torque/power–emissions characteristics of the ICE are affected by coolant temperature T_{ice} and TWC removal efficiency (varying with T_{cat} and λ) significantly. In general, as the engine starts up, the engine heats up, which causes the coolant temperature and TWC temperature to increase. Consequently, the fuel combustion efficiency improves and the TWC removal efficiencies increase, and as a result, the fuel efficiency and emissions improve. Meanwhile, when the engine works, the TWC removal efficiency fluctuates according to the instantaneous A/F ratio.

Taking into account the influence of coolant temperature and catalyst removal efficiency on the HC, CO and NOx emission characteristics, the dynamic emission maps can be derived by the following equation:

$$f_i(n,t) = f_i''(n,t) \cdot \eta_i(T_{\mathrm{ice}}) \cdot \varphi_i(T_{\mathrm{cat}}, \lambda) \tag{1}$$

where $i =$ [HC, CO, NOx], $f_i''(n,t)$ are the hot steady-state emission maps, $\eta_i(T_{\mathrm{ice}})$ are the coolant temperature correction factors, $\varphi_i(T_{\mathrm{cat}}, \lambda)$ are the catalyst removal efficiencies, and $f_i(n,t)$ are the dynamic emission maps of HC, CO, and NOx.

Since the FC and PM are independent of the catalyst removal efficiency, the dynamic FC map and PM emissions map are formulated by the following equation:

$$f_i(n,t) = f_i''(n,t) \cdot \eta_i(T_{\mathrm{ice}}) \tag{2}$$

where $i =$ [FC, PM].

The target of the APU operating point optimization is to improve the fuel efficiency and emissions simultaneously, however, on the speed–torque map of an ICE; the locus of maximum fuel efficiency does not necessarily correspond to the loci of optimum emissions, and there is a definite tradeoff between fuel efficiency and different emissions. Fig. 2 shows a schematic of desired operating locations of a spark ignition (SI) engine.

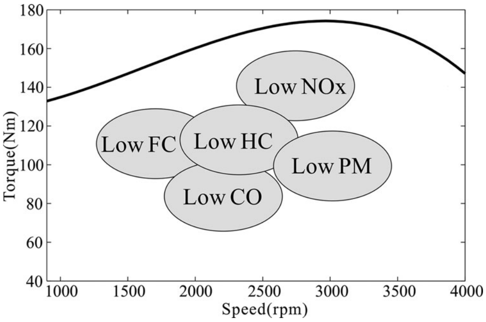

Fig. 2. Fuel efficiency and emissions tradeoffs for an SI engine.

Based on the above analysis, the operating point optimization problem can mathematically be formulated as a multiobjective optimization problem (MOP) as follows:

$$\min_{(n,t)\in\Omega} [f_{\mathrm{HC}}(n,t), f_{\mathrm{CO}}(n,t),$$
$$f_{\mathrm{NOx}}(n,t), f_{\mathrm{FC}}(n,t), f_{\mathrm{PM}}(n,t)] \tag{3}$$

where Ω is the feasible operating area of the APU, which is dependent on the high-level supervisory control strategies.

The goals of minimizing FC and emissions can conflict with each other. The most efficient operating point will likely produce more pollution than less efficient operating points. Moreover, minimizing the amount of one pollutant can increase the amount of another. Recognizing this, the next step of the APU operating point optimization is to allow prioritization of the relative importance of minimizing the FC and each of the pollutants. However, one cannot directly compare FC and emissions because they are in different scales. In order to combine and weight the five metrics, they are first converted to a similar nondimensional scale. To facilitate this, each of the five metrics is normalized to a value between 0 and 1 by the following equation:

$$F_i(n,t) = \frac{f_i(n,t) - \min[f_i(n,t)]}{\max[f_i(n,t)] - \min[f_i(n,t)]} \tag{4}$$

where $i =$ [HC, CO, NOx, FC, PM] and $F_i(n,t)$ are the normalized maps.

Aggregating the objectives to a scalar function and disposed as an single-objective optimization problem is an effective way to solve the MOP. Consequently, the APU dynamic combined cost map is derived by the weighing process

$$F_{\mathrm{CCM}}(n,t) = \frac{\omega_1 F_{\mathrm{HC}} + \omega_2 F_{\mathrm{CO}} + \cdots + \omega_5 F_{\mathrm{PM}}}{\sum\limits_{i=1}^{5} \omega_i}. \tag{5}$$

One benefit of this method is that it is able to establish the relative importance of these constituent factors by adjusting their respective weighting factor. A feasible guideline for weighting factors selection is that preset the weighting factors according to the local emission standards. Due to the fact that different countries have different emission regulations, and these regulations are becoming more and more stringent, it is essential to set different combinations of the weighting factors to meet the local emission standards.

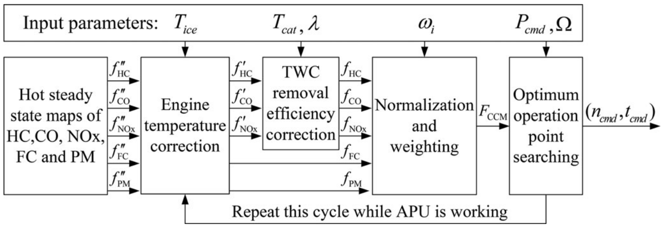

Fig. 3. Schematic of the DCM-based APU operating point optimization approach.

After the dynamic combined cost map is constructed, the APU operating point optimization approach should find out the optimum operating point (n,t) according to the power demands P_{cmd} and searching area instructions Ω from the high-level supervisory control strategy, so that the APU controller manipulates the engine and generator working with high fuel efficiency and low emissions.

The critical steps of the dynamic combined cost map-based APU operating point optimization approach are summarized as follows:

Step 1: Construct the hot steady-state FC and emission maps $f''_{\mathrm{HC}}(n,t)$, $f''_{\mathrm{CO}}(n,t)$, $f''_{\mathrm{NOx}}(n,t)$, $f''_{\mathrm{FC}}(n,t)$ and $f''_{\mathrm{PM}}(n,t)$ through bench tests.

Step 2: Correct the hot steady-state FC and emission maps by applying the coolant temperature correction factors $\eta_i(T_{\mathrm{ice}})$ according to the real-time coolant temperature.

Step 3: Apply the catalyst removal efficiency $\varphi_i(T_{\mathrm{cat}}, \lambda)$ to the engine direct HC, CO, and NOx emissions according to the real-time catalyst temperature and A/F ratio.

Step 4: Normalize the constituent factors by (4) and apply the weighting (5); then, the combined cost map $F_{\mathrm{CCM}}(n,t)$ is derived.

Step 5: Searching the optimum operating point (n,t) in the candidate operating area Ω according to the power demands P_{cmd} of the high-level supervisory control strategy.

The above critical steps of the DCM-based APU operating point optimization approach are graphically demonstrated in Fig. 3.

III. DERIVATION OF THE DYNAMIC COMBINED COST MAP

In this section, the process of constructing the dynamic combined cost map based on the bench test data of real-world engine and motor is discussed step by step.

A. *Hot Steady-State Maps*

The hot steady-state (90 °C of coolant) FC and emission maps (HC, CO, NOx and PM) is derived from the bench test data of a 42-kW naturally aspirated direct injection engine, as shown in Fig. 4(a) – (e). Here, the generator efficiency is also considered. Thus, the fuel efficiency is referred to as fuel-electricity (FE) conversion efficiency, and the FE cost map is introduced by the

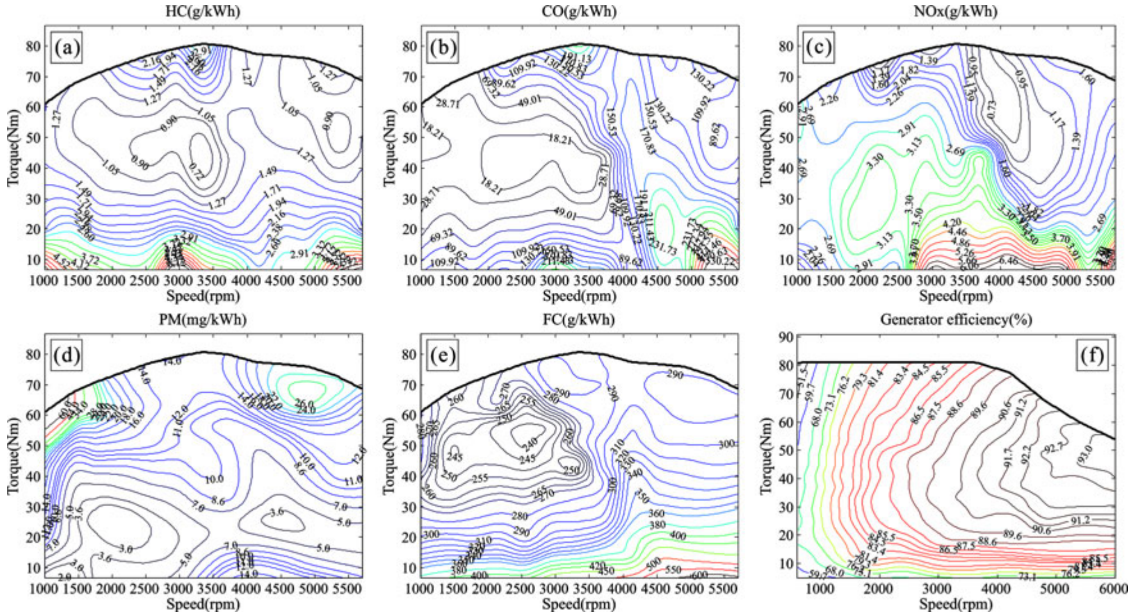

Fig. 4. Hot, steady-state (90 °C of coolant) maps of the engine and generator. (a) HC map. (b) CO map. (c) NOx map. (d) PM map. (e) FC map. (f) Generator efficiency map.

following equation:

$$f''_{\mathrm{FE}}(n,t) = 1 - \frac{360 \cdot f''_{\mathrm{GE}}(n,t)}{f''_{\mathrm{FC}}(n,t) \cdot Q_{\mathrm{LHV}}} \tag{6}$$

where $f''_{\mathrm{FE}}(n,t)$ is the resulted FE cost map, $f''_{\mathrm{GE}}(n,t)$ is the generator efficiency map illustrated in Fig. 4(f) which is derived from the bench test data of a 35-kW PMSM, and Q_{LHV} is the lower heating value of gasoline (4.34×10^7 J/kg). The resulted FE cost map of the APU is shown in Fig. 5. The FE cost is essentially the energy loss ratio in the process of FE conversion. One other thing to note is that the full-load characteristics of the APU are determined by the full-load characteristics of both engine and generator. Thus, the candidate operating area of the APU is the intersection area of the engine full load curve and generator full load curve, as shows in Fig. 5.

B. Coolant Temperature Correction Factors

Engine performance, efficiency, and emissions are significantly affected by the coolant temperature [18]. When the engine is operating at conditions other than fully warm, fuel efficiency and emissions will deteriorated seriously.

In order to quantitatively analyze the influence of the coolant temperature on FC and emissions, the tests are performed on an engine dynamometer where all engine accessories except for oil pump, alternator, and coolant pump are removed. The radiator and thermostat in the cooling system are removed and replaced with a coolant conditioning device (AVL553), which is capable of adjusting the coolant temperature to a desired set point. For every coolant temperature set point, the test is repeated for two New European Driving Cycle (NEDC) driving cycles, the total FC and emissions are measured. The coolant temperature correction factors are defined as

$$\eta_i(T_{\mathrm{ice}}) = \frac{\zeta_i(T_{\mathrm{ice}})}{\zeta_i(90)} \tag{7}$$

where $i =$ [HC, CO, NOx, FC, PM], $\zeta_i(T_{\mathrm{ice}})$ are the total FC and emissions while coolant temperature is set to T_{ice}, and $\zeta_i(90)$ are the total FC and emissions while coolant temperature is set to 90 °C.

For FC, HC, CO, and NOx emissions, the coolant temperature correction factors are then plotted against T_{ice}, as shown in Fig. 6. Curve fitting is used to characterize the coolant temperature correction factors continuously. The curve fitting results of the coolant temperature correction factors are described as follows:

$$\begin{aligned}\eta_i(T_{\mathrm{ice}}) = \;& a_i^0 e^{-0.5((T_{\mathrm{ice}}-a_i^1)/a_i^2)^2} \\ & + b_i^0 e^{-0.5((T_{\mathrm{ice}}-b_i^1)/b_i^2)^2} + c_i^0 T_{\mathrm{ice}} \sin(T_{\mathrm{ice}}) + c_i^1\end{aligned} \tag{8}$$

where $i =$ [HC, CO, NOx, FC, PM], and a_i^0, a_i^1, a_i^2, b_i^0, b_i^1, b_i^2, c_i^0, and c_i^1 are parameters of the fitting results and their exact values are detailed in Appendix A.

When applying the coolant temperature correction factors, it is important to note that the coolant temperature correction factors were developed in a quasi-steady manner, and they cannot represent exactly that of the transient operating conditions of the engine.

C. Catalyst Removal Efficiencies

Since 1980, the TWC has been used to convert harmful emissions of hydrocarbons, carbon monoxide, and oxides of nitrogen into less harmful gases in order to meet the strict emission standards [19]. The removal efficiency of the TWC is strongly

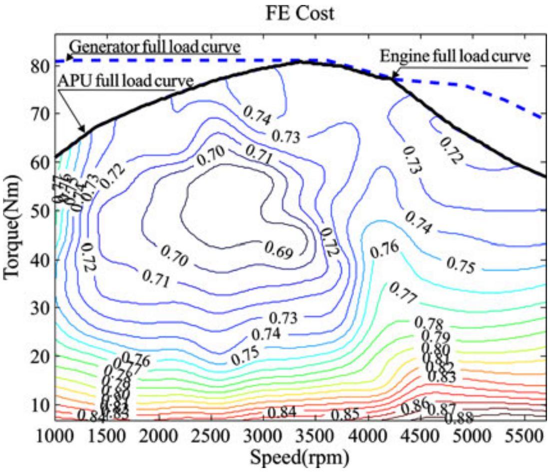

Fig. 5. FE efficiency map of the APU.

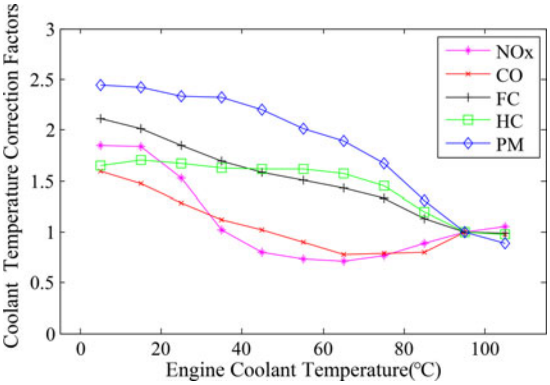

Fig. 6. Engine coolant temperature correction factors.

dependent on the A/F ratio of the exhaust gas and temperature of the catalyst [17], [20].

The removal efficiency of the catalyst δ is defined as follows:

$$\delta = \frac{molin_i - molout_i}{molin_i} \times 100\% \tag{9}$$

where i = [HC, CO, NOx], and $molin_i$ and $molout_i$ are the number of gas moles entering and leaving the TWC, respectively.

The relation between harmful gases removal efficiency and A/F ratio catalyst temperature is formulated as (10) through surface fitting. Fig. 7 shows the fitting surfaces of the HC, CO, and NOx removal efficiency versus λ and T_{cat}:

$$\begin{aligned}\varphi_i(T_{\text{cat}}, \lambda) = \; & p_i^0 \left(0.5 + \arctan\left(\frac{T_{\text{cat}} - p_i^1}{\pi p_i^2}\right)\right) \\ & \cdot \left(0.5 + \arctan\left(\frac{\lambda - p_i^3}{\pi p_i^4}\right)\right)\end{aligned} \tag{10}$$

where i = [HC, CO, NOx], and p_i^0, p_i^1, p_i^2, p_i^3, and p_i^4 are parameters of the fitting results and their exact values are detailed in Appendix B.

D. Normalization and Weighting

The normalization and weighting operations are based on (4) and (5), respectively. When $T_{\text{ice}} = 85$, $T_{\text{cat}} = 350$, and $\lambda = 0.995$, the dynamic combined cost maps with different weighting factors are illustrated in Fig. 8. Fig. 8(a) with $\boldsymbol{\omega} = [0.1, 0.05, 0.05, 0.7, 0.1]$ is mainly created for FC reduction, Fig. 8(b) with $\boldsymbol{\omega} = [0.2, 0.2, 0.2, 0.2, 0.2]$ is a more mixed dynamic combined cost map, in which FC and all hazardous emissions are considered equally important, while Fig. 8(c) with $\boldsymbol{\omega} = [0.1, 0.6, 0.1, 0.1, 0.1]$ mainly aims at CO reduction.

IV. OPTIMUM OPERATING POINT SEARCHING BASED ON PSO

As illustrated in Fig. 8, the contour plots of the dynamic combined cost maps show that the APU operating point optimization problem is a 2-D optimization problem with a large number of local extreme values. To find the optimum operating point in the solution space Ω, the general approach in HEV fields is traversing over the solution space and recording the optimum result [16], [21]. Although simple in arithmetic, it is inefficient and inaccurate. Many optimization approaches have been successfully applied in science and engineering, and these approaches can be classified into two categories: 1) the classic calculus-based approaches, such as Newton's method, steepest descent, and conjugate gradient; and 2) the evolutionary approaches, such as genetic algorithm, differential evolutionary algorithm, and PSO. Compared with the former approaches, the evolutionary approaches have a salient advantage that they do not require restrictive assumptions about solution space, such as continuity, differentiability, and unimodality. Among various of evolutionary approaches, PSO is a remarkable one because its algorithm is conceptually much simpler than other evolutionary approaches and thus demands lower computational costs. This feature is extremely important when the PSO is applied to real-time APU operating point optimization. Furthermore, it has high global convergence speed and local search ability. In view of the above advantages of the PSO, it is utilized to search the optimal APU operating point in this paper.

A. PSO Algorithm

PSO is a population stochastic optimization algorithm developed by Kennedy and Eberhart, who were inspired by the social behavior of bird flocking[22]. It has been used to solve a range of optimization problems, such as parameter identification [23], [24], maximum power point tracking for the photovoltaic system [25], and HEVs parameter optimization [26], [27]. In PSO, all particles fly through the problem space by following the optimum particles. During each iteration, each particle accelerates in the direction of its own personal best solution found so far, as well as in the direction of the global best position discovered so far by any of the particles in the swarm. This means that if a particle discovers a promising new solution, all the other particles will move closer to it, exploring the region more thoroughly in the process [28].

For a d-dimensional optimization problem with swarm size N, in generation k, each individual particle $(1 \leq i \leq N)$ has

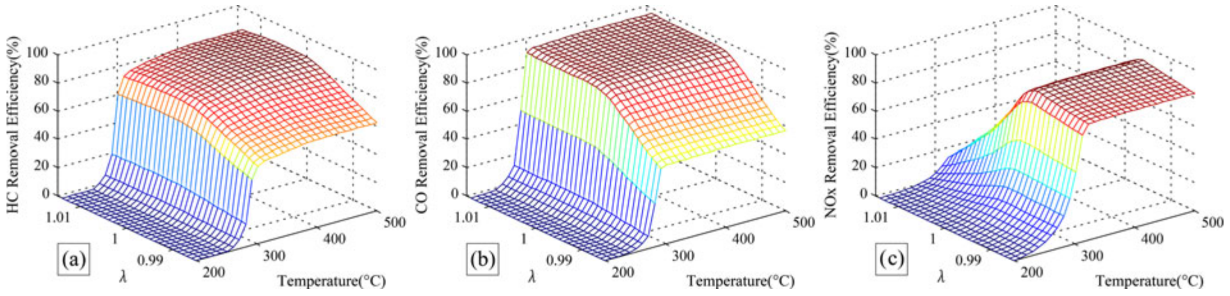

Fig. 7. Curved surfaces of the removal efficiency versus λ and T_{cat}. (a) HC removal efficiency surface. (b) CO removal efficiency surface. (c) NOx removal efficiency surface.

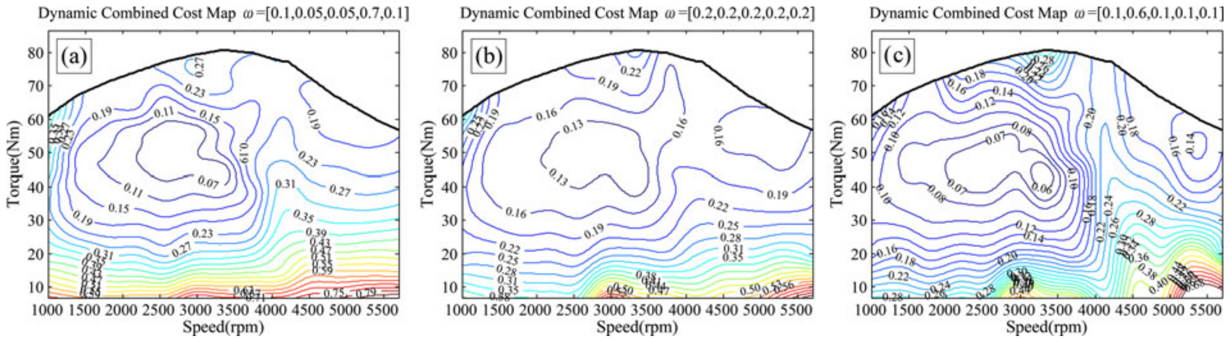

Fig. 8. Dynamic combined cost maps with different weighting factors. (a) $\boldsymbol{\omega} = [0.1,0.05,0.05,0.7,0.1]$. (b) $\boldsymbol{\omega} = [0.2,0.2,0.2,0.2,0.2]$. (c) $\boldsymbol{\omega} = [0.1,0.6,0.1,0.1,0.1]$.

the following attributes: a current position $p_j^i(k)$ in the search space Ω^d, where j is the jth dimension of the particle ($j = 1,\ldots,d$), a current velocity $v_j^i(k)$, and a personal best position $Pb^i = [pb_1^i,\ldots,pb_d^i]$. During each iteration, each particle i in the swarm is updated in the jth dimension using the velocity update formula (11) and the position update formula (12):

$$v_j^i(k+1) = \underbrace{\mu \cdot v_j^i(k)}_{\text{velocity reference}} + \underbrace{\tau_1 r_1 [pb_j^i(k) - p_j^i(k)]}_{\text{individual optima reference}} + \underbrace{\tau_2 r_2 [pg_j(k) - p_j^i(k)]}_{\text{global optima reference}} \tag{11}$$

$$p_j^i(k+1) = p_j^i(k) + v_j^i(k+1). \tag{12}$$

The velocity update formula can be divided into three subformulas, the current velocity reference formula, the individual optima reference formula, and the global optima formula, as shown in the (11), where μ is the inertia weight, r_1 and r_2 are two random values in range [0, 1], and τ_1 and τ_2 are the acceleration coefficients. $Pg = [pg_1,\ldots,pg_d]$ is the global optimal position.

The individual best position of each particle is updated by

$$Pb^i(k+1) = \begin{cases} Pb^i(k), & f[P^i(k+1)] \geq f[Pb^i(k)] \\ P^i(k+1), & f[P^i(k+1)] < f[Pb^i(k)] \end{cases} \tag{13}$$

and the global best position is defined as

$$Pg(k) = \arg\min f[Pb^i(k)], 1 \leq i \leq N. \tag{14}$$

After the positions of all particles are evaluated, corrections are made to the Pb^i and Pg. The optimization program repeats this cycle until the desired objective value is obtained or the maximum iteration number is reached.

B. Optimum Operating Point Searching Based on PSO

According to the different high-level supervisory control strategies, the APU operating point optimization problem can be classified into three main categories: 1) searching the optimum operating point in the whole dynamic combined cost map [2], [4], that is, $\Omega = \mathbb{R}$, where $\mathbb{R}$ means all the feasible operating area of the dynamic combined cost map; 2) searching the optimum operating point in a specific power interval [21], that is, $\Omega = [P_{\mathrm{low}}, P_{\mathrm{high}}]$; and 3) searching the optimum operating point with a specific power value [6], [8], that is, $\Omega = P_{\mathrm{set}}$. For different searching space Ω, the APU operating point optimization problem has different constraints. These constraints must be disposed separately [29].

1) $\Omega = \mathbb{R}$: In this case, the constraints of the APU operating point optimization problem are described as follows:

$$\begin{cases} n_{\min} \leq n \leq n_{\max} \\ t_{\min} \leq t \leq f_{tm}(n) \end{cases} \tag{15}$$

where $n_{\min}$ and $n_{\max}$ are the minimum and maximum speed of the APU, respectively. $f_{tm}(n)$ is the maximum APU torque as shown in Fig. 9, and it can be formulated as (16) through curve

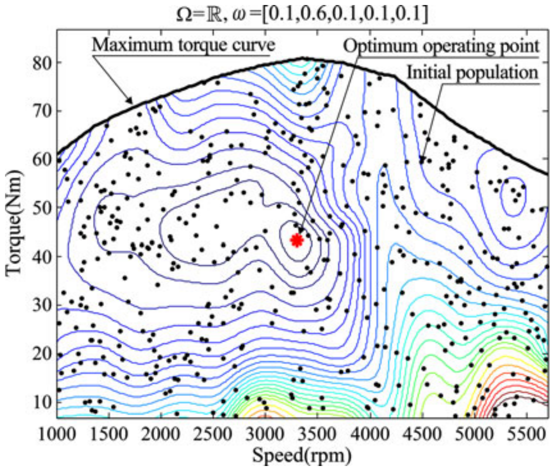

Fig. 9. Maximum torque curve, initial population, and optimum operating point when $\Omega = \mathbb{R}$.

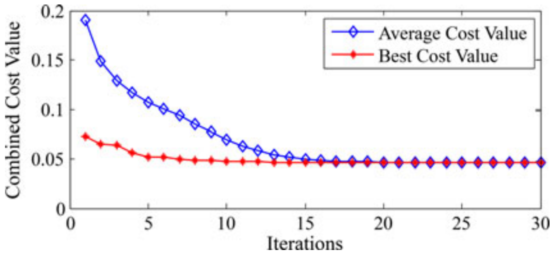

Fig. 10. Average fitness and best fitness profiles.

fitting

$$f_{tm}(n) = \beta_4 n^3 + \beta_3 n^{2.5} + \beta_2 n^2 + \beta_1 n + \beta_0 \tag{16}$$

where $\beta_0, \beta_1, \beta_2, \beta_3$, and β_4 are the polynomial coefficients and their exact values are detailed in Appendix C.

As an example of $\Omega = \mathbb{R}$, for the combined cost map when $T_{\text{ice}} = 85$, $T_{\text{cat}} = 350$, $\lambda = 0.995$, and $\boldsymbol{\omega} = [0.1, 0.6, 0.1, 0.1, 0.1]$, the distribution of the initial population and the optimization result both are shown in Fig. 9, where the parameters of the PSO are set as $\mu = 0.8$, $\tau_1 = 0.2$, $\tau_2 = 0.2$, and $N = 450$. The average cost value and best cost value profiles versus iteration numbers are shown in Fig. 10.

2) $\Omega = [P_{\text{low}}, P_{\text{high}}]$*:* When $\Omega = [P_{\text{low}}, P_{\text{high}}]$, the searching space Ω is restricted to a certain power interval and the constraints are described as

$$\begin{cases} \max(n_{\min}, \Xi_x(f_{tm}(n), g(P_{\text{low}}, n))) \le n \le \\ \quad \min(n_{\max}, \Xi_x(t = t_{\min}, g(P_{\text{high}}, n))) \\ \max(t_{\min}, g(P_{\text{low}}, n)) \le t \le \min(f_{tm}(n), \\ \quad g(P_{\text{high}}, n)) \end{cases} \tag{17}$$

where $\Xi_x(f_{tm}(n), g(P_{\text{low}}, n))$ is the x coordinate of the intersection point of $f_{tm}(n)$ and $g(P_{\text{low}}, n)$, $f_{tm}(n)$ is the APU full load curve, and $g(P, n)$ is a formula that describes the relation between torque and speed when power is P

$$g(P, n) = \frac{30 \cdot P}{\pi n}. \tag{18}$$

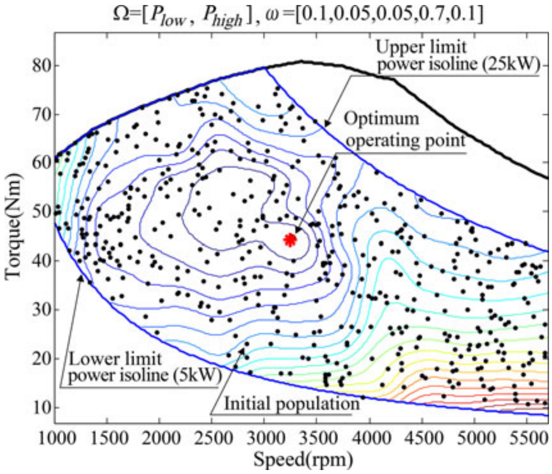

Fig. 11. Initial population, optimum operating point, and upper and lower power isoline when $\Omega = [5, 25]$.

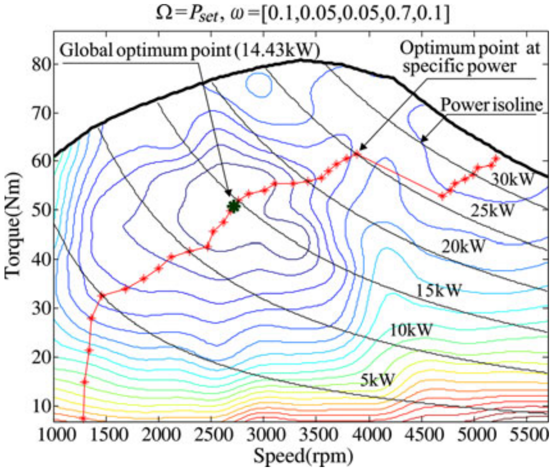

Fig. 12. Optimum operating points at different P_{set} between 1 and 33 kW.

As an example of $\Omega = [P_{\text{low}}, P_{\text{high}}]$, for the combined cost map when $T_{\text{ice}} = 85$, $T_{\text{cat}} = 350$, $\lambda = 0.995$, and $\boldsymbol{\omega} = [0.1,0.05,0.05,0.7,0.1]$, the feasible solution space, initial population distributions, optimum operating point, and upper and lower power isoline are shown in Fig. 11, where $[P_{\text{low}}, P_{\text{high}}] = [5, 25]$ and the population size is set to $N = 25 \cdot (P_{\text{high}} - P_{\text{low}})$.

3) $\Omega = P_{\text{set}}$*:* When $\Omega = P_{\text{set}}$, the APU operating point optimization problem is a 1-D optimization problem, the constraints are described as

$$\begin{cases} n_{\min} \le n \le n_{\max} \\ t = g(P_{\text{set}}, n). \end{cases} \tag{19}$$

In this case, all particles move along the power isoline $t = g(P_{\text{set}}, n)$ and toward the point with the minimum combined cost value. When $T_{\text{ice}} = 85$, $T_{\text{cat}} = 350$, $\lambda = 0.995$, and $\boldsymbol{\omega} = [0.1,0.05,0.05,0.7,0.1]$, the results of the optimum operating points at different P_{set} between 1 and 33 kW with power interval of 1 kW are shown in Fig. 12. The global optimum operating point and some power isolines are also shown in Fig. 12. The combined cost values of different P_{set} are shown

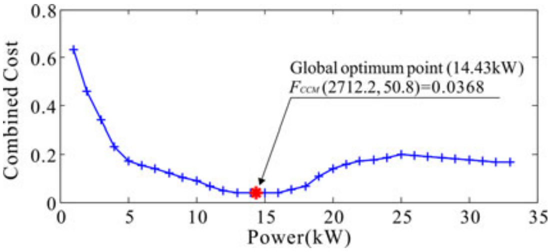

Fig. 13. Combined cost values of different $P_{\rm set}$ between 1 and 33 kW.

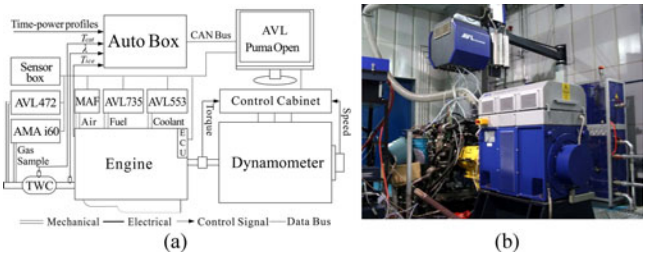

Fig. 14. Schematic diagram and photo of the experimental bench. (a) Schematic diagram. (b) Photo.

in Fig. 13; obviously, the global optimum operating point is $(n, t) = (2712.2, 50.8)$, where the power is 14.43 kW and the minimum combined cost value is 0.0368. Here, the parameters of the PSO are set as: $\mu = 0.8$, $\tau_1 = 0.2$, $\tau_2 = 0.2$, $N = 200$, and the maximum iteration number $t_{\rm max} = 30$.

V. BENCH EXPERIMENT AND RESULTS ANALYSIS

A. *Experimental Facility and Process*

In order to validate the effectiveness of the proposed DCM and PSO-based APU operating point optimization approach, bench experiments are carried out based on the AVL PUMA Open test system. The schematic diagram and photo of the experimental bench are shown in Fig. 14(a) and (b), respectively. The function of each component of the experimental bench is described as follows.

1) *AutoBox:* A rapid control prototyping toolkit. It is a real-time controller with real I/O interfaces. Here, it acts as an APU controller, which implements the APU operating point optimization approach and then outputs the resulted APU operating point (n, t).
2) *AVL Puma Open:* A test bench automation system. It offers an integrated solution for data acquisition and experiment procedure management. Here, it receives speed/torque (n, t) command from the AutoBox through CAN bus and manipulates the dynamometer/engine works in "T/N" mode (defined by AVL, it means that the dynamometer works in torque control mode and engine works in speed control mode);
3) *Dynamometer:* An ac electric dynamometer. Here, it serves as a controllable load of the engine.
4) *Control Cabinet:* An electric device that is used to drive the electric dynamometer according to the torque command of the AVL Puma Open.
5) *AMA i60:* Exhaust measurement device. It reports the HC, CO, and NOx emissions of the engine.
6) *AVL 472:* A partial-flow particulate sample device. It reports the PM emission of the engine.
7) *AVL 735:* Fuel mass flow meter. It reports the FC of the engine.
8) *AVL 553:* Coolant temperature regulating system. It is used to regulate the coolant temperature to 20 °C before each driving cycle.
9) *MAF:* Air mass flow meter. It reports the engine intake air mass flow rate, which is a parameter used in exhaust emission data processing.
10) *Sensor box:* An integrated sensor signal process unit. Here, it used to collect sensor signals such as temperature and humidity of the engine intake air and temperature of the TWC.

The three driving cycles used in the experiment are NEDC, Federal test procedure (FTP), and High way fuel economy test (HWFET). The power following charge depleting (PFCD) strategy is utilized as the high-level supervisory control strategy in the experiment [1]. According to the PFCD, the APU starts immediately when the SOC below its lower desired level $\rm SOC_{min}$. Then, the PFCD sends APU power demand command $P_{\rm cmd}$ to APU controller according to the real-time vehicle power demand. In order to suppress the transient of the engine power, the following limitations are imposed on the APU: the "minimum time engine remains off" is set to 60 s, the "maximum rate of engine power increase" and "maximum rate of engine power decrease" are both set to 0.5 kW/s, and the "minimum power of the APU" is set to 3.75 kW. Here, the higher desired SOC level $\rm SOC_{max}$ is set to 0.7, $\rm SOC_{min}$ is set to 0.3, and the changes in SOC between the beginning and the end of each driving cycle are limited to less than $\pm 0.5\%$, such that the experiment is considered charge-neutral (no net battery energy is consumed over the course of a driving cycle). In the beginning of each driving cycle, the SOC is set to 0.3, such that the APU starts immediately when the "minimum time engine remains off" is reached. The vehicle speed profile, the resulted $P_{\rm cmd}$ profile, battery power $P_{\rm bat}$, and SOC profiles of the NEDC, FTP, and HWFET driving cycles are shown in Fig. 15(a) and (b). It can be seen from Fig. 15(b) that the SOC deviation between the start and end of each driving cycle is very small (0.302% for NEDC, 0.414% for FTP, and 0.107% for HWFET). The battery functions only as a power damper which supplies the peaking power demand of the vehicle and absorbs the charging power from the APU and regenerative braking. In Fig. 15(b), positive $P_{\rm bat}$ represents discharging power and negative $P_{\rm bat}$ represents charging power.

The overall experiment process is described as follows. First, the power demands $P_{\rm cmd}$ of NEDC, FTP, and HWFET driving cycles are calculated according to the vehicle dynamics and PFCD [1]. Here, the vehicle speed profiles and the resulted $P_{\rm cmd}$ profiles of the three driving cycles are shown in Fig. 15(a). Second, the AutoBox determines the real-time APU power demands according to the runtime of the experiment and the $P_{\rm cmd}$ curves, and then, it runs the optimization routines. The resulted APU operating point (n, t) is sent to AVL Puma Open through CAN

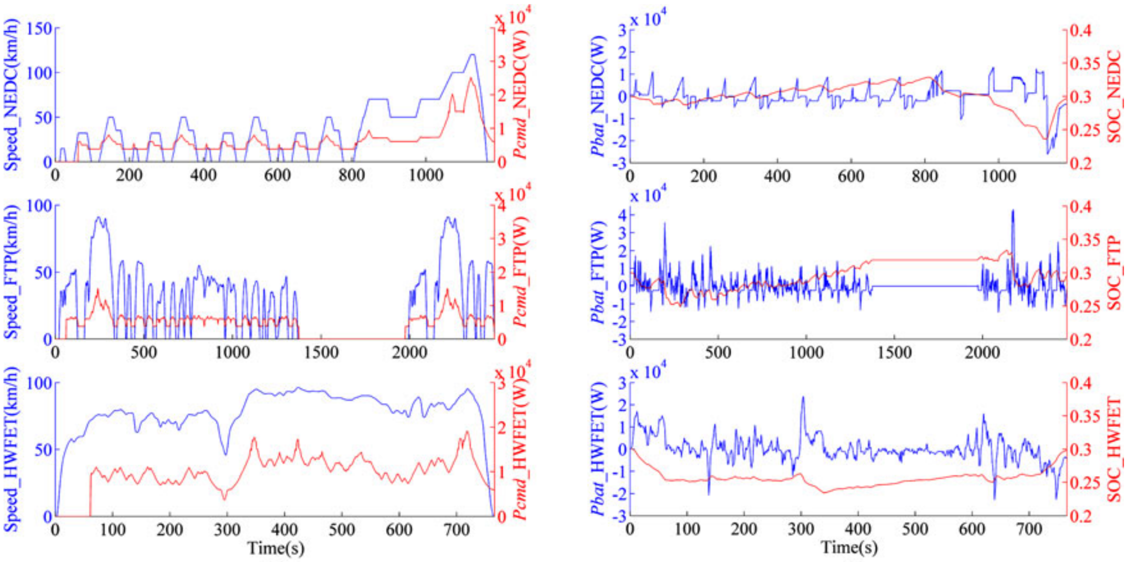

(a) (b)

Fig. 15. Vehicle speed, power demand, battery power, and SOC profiles of the NEDC, FTP, and HWFET driving cycles. (a) Vehicle speed and power demand profiles. (b) Battery power and SOC profiles.

bus. Third, the AVL Puma Open set the experimental bench to "T/N" mode; the expected engine speed n and dynamometer torque t are sent to engine speed regulation unit and the dynamometer control cabinet, respectively. The above process is repeated at a frequency of 1 Hz until the end of the driving cycle is reached. After one driving cycle is completed, the coolant temperature is regulated to 20 °C by AVL 553; the TWC temperature is regulated to 20 °C through natural cooling before the beginning of the next driving cycle.

Here, the proposed approach is compared with the traditional static steady-state FC map (SFM)-based approach. For the SFM-based approach, it shares the same experimental facility and process with the proposed approach, except that the SFM-based approach calculates the APU operating point (n, t) according to the SFM and optimal brake-specific fuel consumption curve.

In the experiment, the parameters of the PSO are set as: $\mu = 0.8$, $\tau_1 = 0.2$, $\tau_2 = 0.2$, $N = 200$, and $t_{\max} = 30$; the weighting factors of the DCM are set to $\omega = [0.1, 0.05, 0.4, 0.4, 0.05]$.

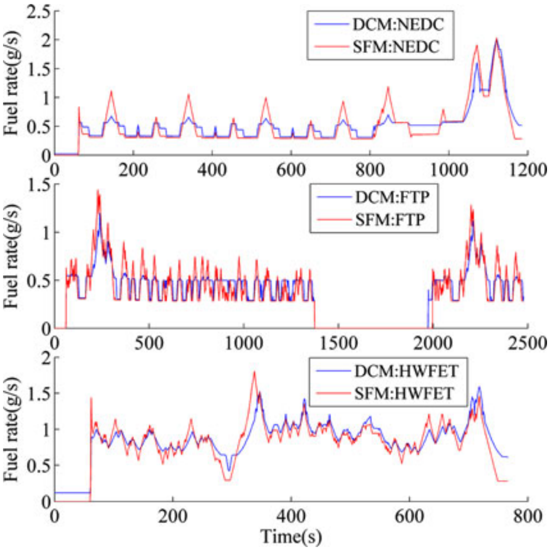

Fig. 16. Fuel rate of the two approaches under NEDC, FTP, and HWFET driving cycles.

B. Experimental Results analysis

The real-time fuel rates of the proposed approach and SFM-based approach are shown in Fig. 16. It can be seen that there is no marked differences between the instantaneous fuel rate of the two approaches. The real-time emission rates of the two approaches are shown in Fig. 17(a) and (b), respectively. Furthermore, since the AVL 472 is a partial-flow particulate sample device and it gives only the total weight of the PM which generated during one test cycle, only the real-time HC, CO, and NOx emission rates are shown in Fig. 17(a) and (b). As can be seen in Fig. 17(a) and (b), the emission rates of the HC, CO, and NOx are relatively very high in the initial phase of each test cycle; this is mainly due to that the catalyst temperature is below the light-off temperature and the removal efficiency is very low. As experiment continues, the catalyst temperature as well as its removal efficiency increases gradually, and the emission rate of the pollutants decreases dramatically. Compared with Fig. 17(a), it can be seen that Fig. 17(b) shows significant reduction in the instantaneous emission rate of NOx. As for the HC and CO, their reduction rates are relatively small compared with that of the NOx.

The quantitative results of total FC, HC, CO, NOx, and PM production of the two approaches are presented in Table I. In the third column of each metric, we compared the experimental results of the SFM-based approach with that of the DCM and PSO-based approach by $\frac{R_{\text{DCM}}-R_{\text{SFM}}}{R_{\text{SFM}}} \times 100\%$, where R_{DCM}

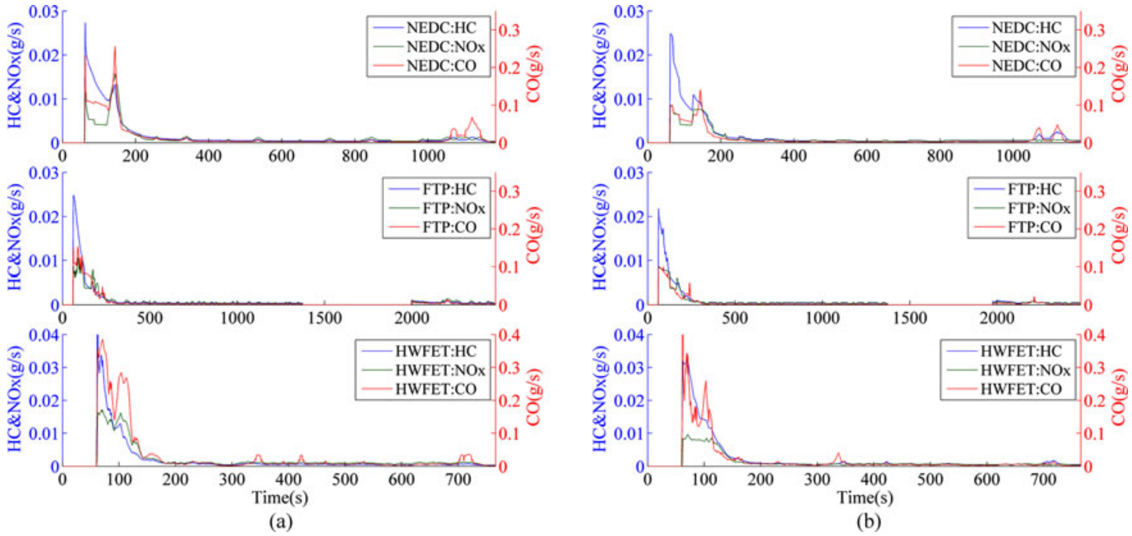

Fig. 17. HC, CO, and NOx emissions under NEDC, FTP, and HWFET driving cycles. (a) Results of the SFM-based approach. (b) Results of the DCM and PSO-based approach.

TABLE I
EXPERIMENTAL RESULTS OF THE TWO APPROACHES

Cycles	FC(L/100km)			HC(g/km)			CO(g/km)			NOx(g/km)			PM(mg/km)		
	SFM	DCM	%	SFM	DCM	%	SFM	DCM	%	SFM	DCM	%	SFM	DCM	%
NEDC	6.32	6.41	1.42	0.108	0.099	−8.43	1.053	0.986	−6.41	0.095	0.074	−22.69	5.3	4.9	−7.55
FTP	7.01	7.15	2.00	0.115	0.111	−3.35	1.09	1.053	−3.35	0.124	0.104	−16.16	6.1	5.9	−3.28
HWFET	4.91	4.98	1.43	0.064	0.055	−13.33	0.883	0.825	−6.52	0.077	0.057	−26.04	3.8	3.7	−2.63
Average	6.08	6.18	1.62	0.095	0.088	−8.36	1.009	0.955	−5.43	0.099	0.078	−21.63	5.1	4.8	−4.49

and R_{SFM} are the experimental results of the two approaches, respectively. According to the technical specification of the experimental bench, the measuring precision of the FC and PM are $\pm 0.12\%$ and $\pm 1\%$, respectively. The measuring precision of the HC, CO, and NOx is $\pm 1\%$. The measuring precision of HC, CO, and NOx is defined as 2.5 times the standard deviation of ten repetitive responses to a given calibration gas. To ensure the measuring accuracy, the AMA i60 is calibrated by using a zero gas and a span gas before and after each driving cycle, and the zero drift, as well as the span drift between the pretest and posttest calibration is less than $\pm 2\%$.

It can be seen from Table I that for all of the three driving cycles, the four air pollutants of the DCM and PSO approach are decreased to different extent compared with that of the SFM-based approach, at the sacrifice of a slight increase in FC (1.62% average). Furthermore, the NOx emissions of the DCM and PSO-based approach are significantly decreased (average 21.63%), while the other emissions (HC, CO, and PM) are slightly decreased (average 8.36% for HC, 5.43% for CO, and 4.49% for PM). This is due to that the weighting factors are set to $\omega_{\mathrm{HC}} = 0.1$, $\omega_{\mathrm{CO}} = 0.05$, $\omega_{\mathrm{NOx}} = 0.4$, $\omega_{\mathrm{FC}} = 0.4$, and $\omega_{\mathrm{PM}} = 0.05$, and the main aim of the DCM is to improve the NOx emissions. The results of NEDC, FTP, and HWFET driving cycles show that the emission reduction rates are positively correlated with the weighting factors. However, for different driving cycles, the emissions reduction rates are different, such as the HC reduction rate for HWFET driving cycle is -13.33%, while for FTP driving cycle, it is only -3.35%. The FC increasing rates vary for different driving cycles too, and for NEDC, FTP, and HWFET driving cycles, they are 1.42%, 2.00%, and 1.43%, respectively. These indicate that the proposed APU operating point method can effectively reduce the HC, CO, and NOx emissions at the expense of a slight drop in fuel efficiency, and the emissions reduction rates are positively correlated with the predefined weighting factors and determined by the specific driving cycle.

VI. CONCLUSION

In this paper, a new methodological approach has been developed for the APU operating point optimization problem. The innovation of the proposed DCM and PSO-based APU operating point optimization approach can be summarized as follows:

1) Recognizing that transient FC and emissions are not only dependent on the hot steady-state maps, but also are significantly affected by the working conditions of engine and TWC, the proposed approach quantitatively analyzes the influence of coolant temperature T_{ice}, catalyst temperature

TABLE II
PARAMETERS OF $\eta_i(T_{\text{ice}})$

Parameters	HC	CO	NOx	FC	PM
a_i^0	0.087225	−1.322934	0.352634	−0.495008	−5.3397
a_i^1	17.413522	76.585893	101.626343	100.070916	90.171155
a_i^2	7.78678	51.156092	−14.996619	16.269422	−1.891372
b_i^0	−0.667302	2.587353	1.214584	0.671653	−2.22426
b_i^1	100.227471	90.824325	10.420419	−1.284121	148.819073
b_i^2	−15.573819	−1.760348	5.807783	24.807007	−52.547185
c_i^0	1.619766	2.093846	0.692571	1.464059	2.49953
c_i^1	6.6921E−5	−0.000141	−0.000157	5.7879E−5	0.00034

T_{cat}, and A/F ratio λ on the speed–torque–fuel efficiency characteristics and speed–torque–emissions characteristics of the APU.

2) Noting that the locus of maximum fuel efficiency on the speed–torque map of an ICE does not necessarily correspond to the loci of optimum emissions and there is a definite tradeoff between high fuel efficiency and low emissions, the dynamic combined cost map is proposed by combining the individual cost maps [FC, HC, CO, NOx, PM] with predefined weighting factors, so as to balance the potentially conflicting goals of FC and emissions reduction in the choice of operating point.
3) In order to search the optimum APU operating point accurately and efficiently, the PSO is introduced and three kinds of constraints are discussed according to which high-level supervisory control strategy of the vehicle is utilized.

The proposed DCM and PSO-based optimization approach is validated in bench experiment over three typical driving cycles. The experimental results show that compared with the SFM-based approach, the results of the DCM and PSO-based optimization approach show significant improvements in the performance of emissions for all of the three tested driving cycles at the expense of a slight drop in fuel efficiency. In the face of growing air pollution, compared with the traditional APU operating point which focuses only on the fuel efficiency and shows little sensitivity to the subtle emissions tradeoffs, the proposed approach opens a new way for the development of APU control strategy, especially in China, where the air quality is almost intolerable. The performance of the proposed APU operating point optimization approach under different combinations of weighting factors, as well as under different high-level supervisory control strategies, is an important topic that requires further research.

APPENDIX

A. $\eta_i(T_{\text{ice}})$

$$\eta_i(T_{\text{ice}}) = a_i^0 e^{-0.5((T_{\text{ice}}-a_i^1)/a_i^2)^2} + b_i^0 e^{-0.5((T_{\text{ice}}-b_i^1)/b_i^2)^2} + c_i^0 T_{\text{ice}} \sin(T_{\text{ice}}) + c_i^1$$

where $i =$ [HC, CO, NOx, FC, PM]; the curve fitting parameters a_i^0, a_i^1, a_i^2, b_i^0, b_i^1, b_i^2, c_i^0, and c_i^1 are detailed in Table II.

TABLE III
PERFORMANCE INDEX OF $\eta_i(T_{\text{ice}})$

Parameters	HC	CO	NOx	FC	PM
RMSE	0.005012	0.015373	0.016817	0.004704	0.015011
SSE	0.000276	0.002599	0.003111	0.000243	0.002479
R	0.999814	0.998309	0.999147	0.999918	0.999618
DC	0.999628	0.99662	0.998294	0.999836	0.999237
Chi-Square	0.000109	0.001238	0.001184	8.991261	0.000555
F-Statistic	24213.821	2653.684	5266.822	54712.981	11781.545

TABLE IV
PARAMETERS OF $\varphi_i(T_{\text{cat}}, \lambda)$

Parameters	HC	CO	NOx
p_i^0	0.94232461	1.07994401	1.01822095
p_i^1	166.36487625	201.08182848	417.33188165
p_i^2	75.17204044	73.68983918	−54.25715017
p_i^3	0.99351848	0.99295057	0.9944181
p_i^4	0.00049265	0.00032866	0.00104812

TABLE V
PERFORMANCE INDEX OF $\varphi_i(T_{\text{cat}}, \lambda)$

Parameters	HC	CO	NOx
RMSE	0.02073319	0.02364406	0.03877321
SSE	0.38687883	0.50313725	1.35302541
R	0.99857771	0.99806104	0.99339897
DC	0.99643333	0.99612582	0.98683841
Chi-Square	4.19694382	2.29775829	2.91330977
F-Statistic	315013.595885	230893.641724	67346.957342

TABLE VI
PARAMETERS AND PERFORMANCE INDEX OF $f_{tm}(n)$

Parameters		Performance index	
β_0	269.09425341	RMSE	1.11575721
β_1	−0.43572528	SSE	39.8372526
β_2	0.00072648	R	0.99774424
β_3	−1.6969E−5	DC	0.99549356
β_4	1.1138E−7	Chi-Square	0.13707131
–	–	F-Statistic	6627.142718

The performance indexes of the fitting results are shown in Table III, where RMSE is the root-mean-square error, SSE is the sum of square error, R is the correlation coefficients, and DC is the determination coefficient.

B. $\varphi_i(T_{\text{cat}}, \lambda)$

$$\varphi_i(T_{\text{cat}}, \lambda) = p_i^0 \left(0.5 + \arctan\left(\frac{T_{\text{cat}} - p_i^1}{\pi p_i^2}\right)\right) \cdot \left(0.5 + \arctan\left(\frac{\lambda - p_i^3}{\pi p_i^4}\right)\right)$$

where $i =$ [HC, CO, NOx]; the surface fitting parameters p_i^0, p_i^1, p_i^2, p_i^3, and p_i^4 are detailed in Table IV.

The performance indexes of the surface fitting results are shown in Table V.

C. $f_{tm}(n)$

$$f_{tm}(n) = \beta_4 n^3 + \beta_3 n^{2.5} + \beta_2 n^2 + \beta_1 n + \beta_0.$$

The curve fitting parameters β_0, β_1, β_2, β_3, and β_4 and the performance indexes are shown in Table VI.

REFERENCES

[1] M. Ehsani, Y. Gao, and A. Emadi, *Modern Electric, Hybrid Electric, and Fuel Cell Vehicles: Fundamentals, Theory, and Design*, 2nd ed., Boca Raton, FL, USA: CRC Press, 2010.

[2] J. Gao, F. Sun, H. He, G. G. Zhu, and E. G. Strangas, "A comparative study of supervisory control strategies for a series hybrid electric vehicle," in *Proc. Asia-Pacific Power Energy Eng. Conf.*, 2009, pp. 1–7.

[3] P. Pisu and G. Rizzoni, "A comparative study of supervisory control strategies for hybrid electric vehicles," *IEEE Trans. Control Syst. Technol.*, vol. 15, no. 3, pp. 506–518, May 2007.

[4] S. Barsali, C. Miulli, and A. Possenti, "A control strategy to minimize fuel consumption of series hybrid electric vehicles," *IEEE Trans. Energy Convers.*, vol. 19, no. 1, pp. 187–195, Mar. 2004.

[5] S. Barsali, M. Ceraolo, and A. Possenti, "Techniques to control the electricity generation in a series hybrid electrical vehicle," *IEEE Trans. Energy Convers.*, vol. 17, no. 2, pp. 260–266, Jun. 2002.

[6] M. Gokasan, S. Bogosyan, and D. J. Goering, "Sliding mode based powertrain control for efficiency improvement in series hybrid-electric vehicles," *IEEE Trans. Power Electron.*, vol. 21, no. 3, pp. 779–790, May 2006.

[7] G. Fiengo, L. Glielmo, and F. Vasca, "Control of auxiliary power unit for hybrid electric vehicles," *IEEE Trans. Control Syst. Technol.*, vol. 15, no. 6, pp. 1122–1130, Nov. 2007.

[8] H. Yoo, S. K. Sul, Y. Park, and J. Jeong, "System integration and power-flow management for a series hybrid electric vehicle using supercapacitors and batteries," *IEEE Trans. Ind. Appl.*, vol. 44, no. 1, pp. 108–114, Jan./Feb. 2008.

[9] M. Demirci, A. Biliroglu, M. Gokasan, and S. Bogosyan, "Sliding mode optimum control for APU of series hybrid electric vehicles," in *Proc. IEEE Int. Symp. Ind. Electron.*, 2010, pp. 340–345.

[10] N. Schofield and A. Al-Adsani, "Operation of a hybrid PM generator in a series hybrid EV power-train," in *Proc. IEEE Veh. Power Propulsion Conf.*, 2011, pp. 1–6.

[11] C. E. Nino-Baron, A. R. Tariq, G. Zhu, and E. G. Strangas, "Trajectory optimization for the engine-generator operation of a series hybrid electric vehicle," *IEEE Trans. Veh. Technol.*, vol. 60, no. 6, pp. 2438–2447, Jul. 2011.

[12] A. Konev and L. Lezhnev, "Control strategy optimization for a series hybrid vehicle," SAE Paper No. 2006-01-0663.

[13] J. Moreno, M. E. Ortzar, and J. W. Dixon, "Energy-management system for a hybrid electric vehicle, using ultracapacitors and neural networks," *IEEE Trans. Ind. Electron.*, vol. 53, no. 2, pp. 614–623, Apr. 2006.

[14] I. M. Panahi and H. A. Toliyat, "An efficient processor-based online generation of time-optimal trajectories," *IEEE Trans. Control Syst. Technol.*, vol. 14, no. 5, pp. 966–973, Sep. 2006.

[15] F. R. Salmasi, "Control strategies for hybrid electric vehicles: Evolution, classification, comparison, and future trends," *IEEE Trans. Veh. Technol.*, vol. 56, no. 5, pp. 2393–2404, Sep. 2007.

[16] V. H. Johnson, K. B. Wipke, and D. J. Rausen, "HEV control strategy for real-time optimization of fuel economy and emissions," SAE Paper No. 2000-01-1543.

[17] E. P. Brandt, Y. Wang, and J. W. Grizzle, "Dynamic modeling of a three-way catalyst for SI engine exhaust emission control," *IEEE Trans. Control Syst. Technol.*, vol. 8, no. 5, pp. 767–776, Sep. 2000.

[18] T. Santhosh, S. Agam, R. Ranjeet, and M. Saravanan, "Investigation on the effect of coolant temperature on the performance and emissions of naturally aspirated gasoline engine," SAE Paper No. 2011-26-0089.

[19] E. Brandt and J. Grizzle, "Three-way catalyst diagnostics for advanced emissions control systems," in *Proc. Am. Control Conf.*, vol. 5, 2001, pp. 3305–3311.

[20] G. Fiengo, J. Grizzle, J. A. Cook, and A. Y. Karnik, "Dual-UEGO active catalyst control for emissions reduction: Design and experimental validation," *IEEE Trans. Control Syst. Technol.*, vol. 13, no. 5, pp. 722–736, Sep. 2005.

[21] V. Sezer, M. Gokasan, and S. Bogosyan, "A novel ECMS and combined cost map approach for high-efficiency series hybrid electric vehicles," *IEEE Trans. Veh. Technol.*, vol. 60, no. 8, pp. 3557–3570, Oct. 2011.

[22] J. Kennedy and R. Eberhart, "Particle swarm optimization," in *Proc. IEEE Int. Conf. Neural Netw.*, 1995, pp. 1942–1948.

[23] Q. Li, W. Chen, Y. Wang, S. Liu, and J. Jia, "Parameter identification for PEM fuel-cell mechanism model based on effective informed adaptive particle swarm optimization," *IEEE Trans. Ind. Electron.*, vol. 58, no. 6, pp. 2410–2419, Jun. 2011.

[24] J. J. Soon and K. S. Low, "Photovoltaic model identification using particle swarm optimization with inverse barrier constraint," *IEEE Trans. Power Electron.*, vol. 27, no. 9, pp. 3975–3983, Sep. 2012.

[25] K. Ishaque, Z. Salam, M. Amjad, and S. Mekhilef, "An improved particle swarm optimization (PSO)-based MPPT for PV with reduced steady-state oscillation," *IEEE Trans. Power Electron.*, vol. 27, no. 8, pp. 3627–3638, Aug. 2012.

[26] X. Wu, B. Cao, J. Wen, and Y. Bian, "Particle swarm optimization for plug-in hybrid electric vehicle control strategy parameter," in *Proc. IEEE Veh. Power Propulsion Conf.*, 2008, pp. 1–5.

[27] C. K. Samanta, S. K. Padhy, S. P. Panigrahi, and B. K. Panigrahi, "Hybrid swarm intelligence methods for energy management in hybrid electric vehicles," *IET Electr. Syst. Transp.*, vol. 3, no. 1, pp. 22–29, 2013.

[28] F. Van den Bergh and A. P. Engelbrecht, "A cooperative approach to particle swarm optimization," *IEEE Trans. Evol. Comput.*, vol. 8, no. 3, pp. 225–239, Jun. 2004.

[29] J. Robinson and Y. Rahmat-Samii, "Particle swarm optimization in electromagnetics," *IEEE Trans. Antennas Propag.*, vol. 52, no. 2, pp. 397–407, Feb. 2004.

Yaonan Wang received the B.S. degree in computer engineering from East China Technology Institute (ECTI), Taiyuan, China, in 1981, and the M.S. and Ph.D. degrees in control engineering from Hunan University, Changsha, China, in 1990 and 1994, respectively.

From 1998 to 2000, he was a Senior Humboldt Fellow in Germany, and from 2001 to 2004, he was a Visiting Professor with the University of Bremen, Bremen, Germany. Since 1995, he has been a Professor with the College of Electrical and Information Engineering, Hunan University. His research interests include hybrid electric vehicle control, power plant control, and intelligent control theory and its applications.

Yongpeng Shen was born in Henan, China, in 1985. He received the B.S. and M.S. degrees in electrical engineering from Zhengzhou University of Light Industry, Zhengzhou, China, in 2007 and 2010 respectively. He is currently working toward the Ph.D. degree with the College of Electrical and Information Engineering, Hunan University, Changsha, China.

His research interests include electric machine control, hybrid electric vehicle optimization, and control.

Xiaofang Yuan was born in Hunan, China, in 1979. He received the B.S., M.S., and Ph.D. degrees in electrical engineering from Hunan University, Changsha, China, in 2001, 2006, and 2008, respectively.

In 2008, he joined the College of Electrical and Information Engineering, Hunan University, where he is currently an Associate Professor. His research interests include wireless power transmission and hybrid electric vehicle control. He has authored or coauthored more than 30 refereed papers.

Dr. Yuan received the Second-Grade National Awards at the Science and Technology Progress of China in 2009.

Yimin Yang received the M.S. and Ph.D. degrees in electrical engineering from Hunan University, Changsha, China, in 2009 and 2013, respectively.

He is currently an Assistant Professor at the College of Electric Engineering, Guangxi University, Nanning, China. He is also a Postdoctoral Fellow with the Department of Electrical and Computer Engineering, University of Windsor, Canada.

His research interests mainly include machine learning and its application in electric vehicle drivetrain control.